Implications of terrain resolution on modeling rainfall-triggered landslides using a TIN-based model

E. Arnone[1], A. Francipane[2], Y.G. Dialynas[3,4], L.V. Noto[2], R.L. Bras[5]

[1] Dipartimento Politecnico di Ingegneria e Architettura, Università degli Studi di Udine, Udine, ITALY
[2] Dipartimento di Ingegneria, Università degli Studi di Palermo, Palermo, ITALY
[3] Department of Civil and Environmental Engineering, University of Cyprus, Nicosia, CYPRUS
[4] Nireas-International Water Research Centre, University of Cyprus, P.O. Box 20537, 1678 Nicosia, Cyprus
[5] School of Civil and Environmental Engineering, Georgia Institute of Technology, Atlanta, USA

Corresponding author: Dr. Elisa Arnone, elisa.arnone@uniud.it

Dipartimento Politecnico di Ingegneria e Architettura, Università degli Studi di Udine

Via del Cotonificio, 114 - 33100, Udine, ITALY – phone number: +39 0432 558767

Highlights

- Impacts of five grid-DEM resolutions on hydrologic-stability modeling are assessed
- The model uses Triangulated Irregular Networks to describe the topography
- We analyze direct and indirect effects of hydro-geomorphic processes involved
- Resolution impacts triggering processes when lateral water exchanges are allowed

Abstract

This study employs a distributed eco-hydrological-landslide model, the tRIBS-VEGGIE-Landslide, to evaluate the influence of terrain resolution on the hydro-geomorphological processes involved in slope stability analysis. The model implements a Triangulated Irregular Network (TIN) to describe the topography starting from a grid-DEM. Five grid-DEM resolutions of the case study basin, i.e., 10, 20, 30 and 70 m, are used to derive the corresponding TINs. The results show that using irregular meshes reduces the loss of accuracy with coarser resolutions in the derived slope distribution in comparison to slope distributions estimated from the original grid-based DEM. From a hydrological perspective, the impact of resolution on soil moisture patterns and on slope stability is significant mostly when lateral water exchanges are allowed. The degrading of resolution leads to a reduction of the predicted unstable areas, with respect to the highest resolution case, from about 15% (20 m) to more than 40% (70 m).

Keywords: hydrologic modeling; landslides; numerical modeling; digital elevation models; slope stability analysis.

1 Introduction

Physically-based modeling is one of the approaches used to assess the vulnerability of natural basins to hillslope instability induced by extreme or prolonged precipitation. The increasing trend of weather-related disasters (Hoeppe, 2016) motivates the continuing interest in more reliable tools for prediction and analysis of precipitation-induced landslide events.

One of the issues extensively discussed in landscape modeling is the use of the appropriate grid Digital Elevation Model (DEM) resolution. Specifically, the question is whether adopting the finest available grid-DEM (hereinafter simply DEM) resolution is a justified choice, not only in terms of computational requirements, but also in terms of effective improvement of the model capability in predicting/determining the initiation of landslides (Cavazzi et al., 2013; Fuchs et al., 2014).

The DEM is used to extract morphological secondary attributes, such as slope, aspect, flow path, upstream contributing area, etc. Lack of accuracy in the primary attribute (i.e., elevation) would be propagated on the extracted morphological information (Wu et al., 2007; Vaze et al., 2010; Yang et al., 2014).

In landslide modeling, the local slope angle is the variable which most influences the calculation of the terrain stability, in both direct and indirect ways. Hydrological-stability approaches are based on the integration of distributed hydrological models with the simple infinite slope model (Montgomety and Dietrich, 1994; Iverson 2000, Claessens et al., 2005; Rosso et al., 2006; Arnone et al., 2011; Lepore et al., 2013). The landslide stability model computes the equilibrium of forces on a shallow soil prism. Gravity acts to initiate a slide as a function of the slope angle and the total wight of the soil, including water. Friction resists sliding and it is affected by soil moisture. The steeper the slope, the greater the component favoring slide initiation (direct effect). Catchment slope distribution also controls many of the hydrological terrain-based processes, such as the surface flow paths and the lateral redistribution of subsurface flows, which ultimately determine the local soil moisture, the duration of the transient regime after an event and thus the soil water pressures that impact the forces equilibrium.

Although high resolution digital terrain data allows a more realistic representation of topography and, consequently, a better analysis of hillslope and valley morphology, which are very important in the recognition of the topographic signature of valley incision by debris flows and landslides (Tarolli and Dalla Fontana, 2009), a high resolution DEM does not always imply a better performance in modelling the processes that lead to landslides. Several studies have explored how the grid-cell size of the input topography data may influence rainfall induced landslides. Some studies focus on landslide susceptibility (Chang et al., 1991; Lee and Lin, 2010; Grohmann et al., 2015; Arnone et al., 2016a; Cama 2016) and others explore the impact of resolution on results from physically-based models (Zhang and Montgomery, 1994; Tarolli and Tarboton, 2006; Claessens et al., 2005; De Sy et al., 2013; Keijsers et al., 2011; Fuchs et al., 2014; Penna et al. 2014; Mahaigam and Olsen 2015; Viet et al., 2016). Most of the results of these studies agree that the coarser resolutions tend to smooth the terrain description, i.e., local slope angle decreases, thus reducing the number of unstable areas.

Specifically, Keijsers et al. (2011) used the LAPSUS-LS (Claessens et al., 2005) model and found that coarser resolutions reduced the ability to predict probability of failure at a particular location, yet stable areas were predicted correctly. However, many others concluded that the finest available resolution does not necessarily lead to better model performance (Arnone et al., 2016b; Fuchs et al., 2014), since modelling a physical process such as landslides, may depend on scales not detected with very high resolutions (Tarolli and Tarboton, 2006; Penna et al., 2014). At finer resolutions, the local surface topography is less representative of the process governing the landslide initiation and hence impacts the average size of the landslides (Freer et al., 2002; Tarolli and Tarboton, 2006). The availability of very-high resolutions DEMs (up to 1 m) (Yang et al., 2014; Noto et al., 2017; Francipane et al., 2020) resulting from the use of LIDAR begs the question of their value in landslide mapping (Wang et al., 2013; Fuchs et al., 2014; Ciampalini et al., 2016). Fuchs et al. (2014) found an improvement of 3% in determining slope instability by using < 10 m resolution, but they stated that such an improvement can have a small impact in applications where, for example, the soil terrain properties are poorly described and there is a lack of other data.

All studies mentioned so far make use of hydrological-landslide models that are grid-based, i.e., they require a grid-DEM to describe topography. Another class of hydrological and geomorphologic models uses Triangulated Irregular Networks (TINs) (e.g., CHILD by Tucker et al., 1999; tRIBS by Ivanov et al., 2004; tRIBS-Erosion by Francipane et al., 2012; CHM by Marsh et al., 2020), which make it possible to represent more efficiently the topography by increasing the number of nodes only where morphology is complex. TIN meshes can be built directly from measured elevation points but are more commonly derived from readily available grid-DEMs. Although the quality of simulations directly depends on the TIN mesh, the quality of the TIN discretization depends on the original DEM.

This study evaluates the influence of the DEM resolution on the slope stability analysis by using a distributed eco-hydrological-landslide model, which uses TINs derived from a DEM to describe the topography. Most hydrological-landslide models in the literature are grid-based and not much is written about the dependence of TIN- based models on terrain resolution. We use the tRIBS-VEGGIE-Landslide (Triangulated Irregular Network (TIN)-based Real-time Integrated Basin Simulator - VEGetation Generator for Interactive Evolution) (Lepore et al., 2013), which is capable of representing vegetation dynamics, and rainfall triggered landslides while simulating soil moisture evolution on the hillslope. The study addresses questions regarding the impact of the original DEM resolution on the landslide modeling, for given DEM-TIN conversion algorithm. Some of the questions are: How significant is the influence of the grid resolution on the estimation of slope distribution? How do the resolution impact terrain-driven hydrological processes, such as lateral redistribution, and then the landslide occurrence? How does the use of coarse resolutions modify the amount of the predicted total failure area?

The study area is the Mameyes basin, which is located in the Luquillo Experimental Forest (Puerto Rico), where numerous slope stability analyses have been carried out with the same model (Lepore et al., 2013, Dialynas et al., 2016; Arnone et al., 2016b). The impact of the original DEM resolution on tRIBS–VEGGIE landslide output is studied using different resampled DEMs at 20, 30, 50, and 70 m resolution (from the available 10 m DEM) to obtain the triangulated irregular network required by the model.

2 Methods

2.1 *tRIBS-VEGGIE-Landslide model*

The tRIBS-VEGGIE-Landslide model (Lepore et al., 2013) couples the eco-hydrological model tRIBS-VEGGIE (Ivanov et al., 2008) and the infinite slope analysis in order to compute the factor of safety (*FS*) of a slope as a response to the soil moisture dynamics.

The hydrological component of the model reproduces essential hydrologic processes over the complex topography of a river basin (e.g., infiltration, evapotranspiration, interception, lateral redistribution and soil moisture dynamics). It considers spatial variability in precipitation fields and the land surface and computes the corresponding soil moisture dynamics. The role of topography in lateral soil moisture redistribution is emphasized by taking into account the effects of heterogeneous and anisotropic soil. Topography is described by means of a multiple-resolution approach based on a TIN, which offers a flexible computational structure that reduces the number of computational elements without a significant loss of information (Vivoni et al., 2004) and hence increasing the computational performance of the model.

The vegetation module simulates the biophysical energy processes (e.g., transpiration), biophysical hydrologic processes (e.g., vegetation dependent unsaturated soil moisture), and biochemical processes (e.g., photosynthesis and plant respiration).

In addition to the soil moisture in the unsaturated zone and water table dynamics, the stability model accounts also for the soil-water characteristic curve and the saturated shear strength parameters (cohesion and friction angle) to assess *FS*. The implemented equation is the following:

$$FS(t) = \frac{c'}{\gamma_s z_n sin\alpha} + \frac{tan\phi}{tan\alpha} - \frac{\gamma_w \Psi_b}{\gamma_s z_n}\left(\frac{\theta(t)-\theta_r}{\theta_s-\theta_r}\right)^{1-\frac{1}{\lambda}} \cdot \frac{tan\phi}{sin\alpha} \quad \text{(eq. 1)}$$

where *FS* (*t*) is the time-dependent factor of safety (hereinafter simply *FS*); c' is the effective soil cohesion; γ_s is the total unit weight of soil, which varies with soil moisture; γ_w is the water unit weight; z_n is the soil depth along the normal direction to the slope; α and ϕ are the slope and the soil friction angle, respectively; ψ_b is the air entry bubbling pressure (assumed negative); λ is the pore-size distribution index; θ (*t*) is the time-dependent volumetric water content (hereinafter simply θ); θ_r and θ_s are the residual and saturated soil moisture contents, respectively. ψ_b and λ are the parameters of the Brooks and Corey formulation (1964) which relate hydraulic conductivity and soil water potential to soil moisture (Sivandran and Bras, 2012). Under the condition in which soil is full of water down to the considered soil depth, eq. 1 reduces to the saturated conditions formulation (Arnone et al., 2016).

The final products of the module are dynamic maps of instability areas as well as dynamic *FS* depth profiles at selected areas, which depend on soil moisture dynamics.

More information about the formulation used in the slope stability model can be found in Lepore et al. (2013) and Arnone et al. (2016b), while for more details about tRIBS-VEGGIE the reader can refer to Ivanov et al. (2008).

2.2 *Terrain analysis algorithms*

The most common methods to represent terrain data are DEMs and triangulated irregular networks, which can be easily incorporated into geographical information systems (GIS) and are increasingly used as data input for hydrological, hydraulic, and morphological models (Goodrich et al., 1991; Kumler 1994; Mita et al., 2001; Tucker et al., 2001; Ivanov et al., 2004a, b). TINs are used since they make possible the representation of very complex topography in a very efficient way. Areas of uniform terrain can be represented with few triangular elements, while complex areas can be represented with increased details by using more triangular elements (Goodrich et al., 1991). TINs are extraordinarily flexible and resilient in the representation of terrain.

In order to build an appropriate TIN, it is very important to decide how to pick the sample points from the original dataset and/or how to triangulate them. One of the most important and used triangulation methods is the Delaunay Triangulation (DT) (Watson and Philip 1984; Tsai 1993). It is the dual graph of the Voronoi diagram, also called Thiessen polygons, which subdivides the space into a set of convex polygons whose boundaries are the perpendicular bisectors between adjacent data points. The dual relationship between DT and its Voronoi diagram provides a direct solution to the nearest neighbor problem for a set of points in such a way that each triangle vertex is connected to its nearest neighbors.

The algorithm used in this work to convert a DEM into a TIN is the one implemented within the TIN Index Analysis Package (Vivoni et al. 2004) (TIAP - http://vivoni.asu.edu/tribs/tinindex.html), which allows the user to obtain a hydrologically-significant TIN from a high-resolution DEM (e.g., LIDAR) suitable for models such as tRIBS-Veggie-Landslide. The package can derive a TIN from a DEM by means of two different 'target' methods: the TIN Index method, which is based on the idea of hydrologic similarity, and the TIN Terrain or Slope Criteria method, which is instead based on the topographic relevance of DEM points in describing the terrain. The terrain-based approach uses a higher resolution for rugged terrain areas while flatter areas have a lower resolution. For the sampling of DEM points, the package provides three different point selection methods: *proximal distance* (PD), *very important points* (VIP) and *latticetin* (LT). The LT sampling method (Lee, 1991) is used here, because it preserves the catchment slope distribution in a robust and more accurate manner than the others (e.g., Vivoni et al., 2004). Starting from a DEM, this method retains all those points that are required for maintaining a surface within a specified elevation tolerance that reflects the maximum allowable difference in elevation between the input grid and the surface created from the output TIN.

The generation of an appropriate terrain model for hydrological purposes should ensure that the TIN conforms to the watershed boundary and the watershed stream network. The created TIN mesh thus allows for flow and transport from a node to another, along triangle edges, using a finite difference approach. Hydrologic processes (e.g., infiltration, evaporation, groundwater table elevation) are computed on the Voronoi polygon associated with each node. Slope is calculated based on the TIN, along each triangle edge. A slope value is assigned to a Voronoi polygon along the steepest of the spokes connected to the Voronoi node. The slope is used to define the drainage flow path originating from each computational node (Braun and Sambridge, 1997; Tucker et al. 1999; Vivoni et al., 2004).

3 Study case

3.1 *Basin* description

The Mameyes basin is within the Luquillo Experimental Forest (LEF), in the northeast of the island of Puerto Rico, USA. It has an area of 16.7 km^2, with an elevation ranging between 104.2 and 1,046 m a.s.l. (Figure 1a). About 30% of the basin has a slope greater than 25 deg (Figure 1a). The basin is one of the wettest basins in Puerto Rico and is characterized by a high variability in rainfall and air temperature throughout the basin. The mean annual precipitation (MAP) ranges between 3,000 and 5,000 mm. High percentages of sandy-loam and clay-loam, with lower percentages of clay and silty-clay, make up the soil of the basin. The bedrock is located at a depth of about 8 m or deeper (Simon et al., 1990) and does not affect the shallow slope failure mechanisms. Vegetation is mainly made of tabonuco forest (*Dacryodes excelsa*), typically within 150 and 600 m of elevation, colorado forest (*Cyrilla racemiflora*), within 600 and 900 m of elevation, and dwarf (cloud) forest, above 900 m. In addition, the palm forest (*Prestoea montana*) is usually present on steep and poorly drained sites.

The Mameyes basin has been selected as a case study because the availability of data to implement tRIBS-VEGGIE and the large number of landslides, which make the basin a good test case for the tRIBS-VEGGIE-Landslide. As an example, Hurricane Maria, which hit Puerto Rico in September 2017, caused about 20 landslides across the basin (Figure 1a). Figure 1b shows images of three landslides that occurred along the PR-191 road and observed during a field trip in the Rio Mameyes basin in 2014. Also shown is an old landslide with new vegetation.

More information about the study area can be found in Lepore et al. (2013) and Arnone et al. (2016b).

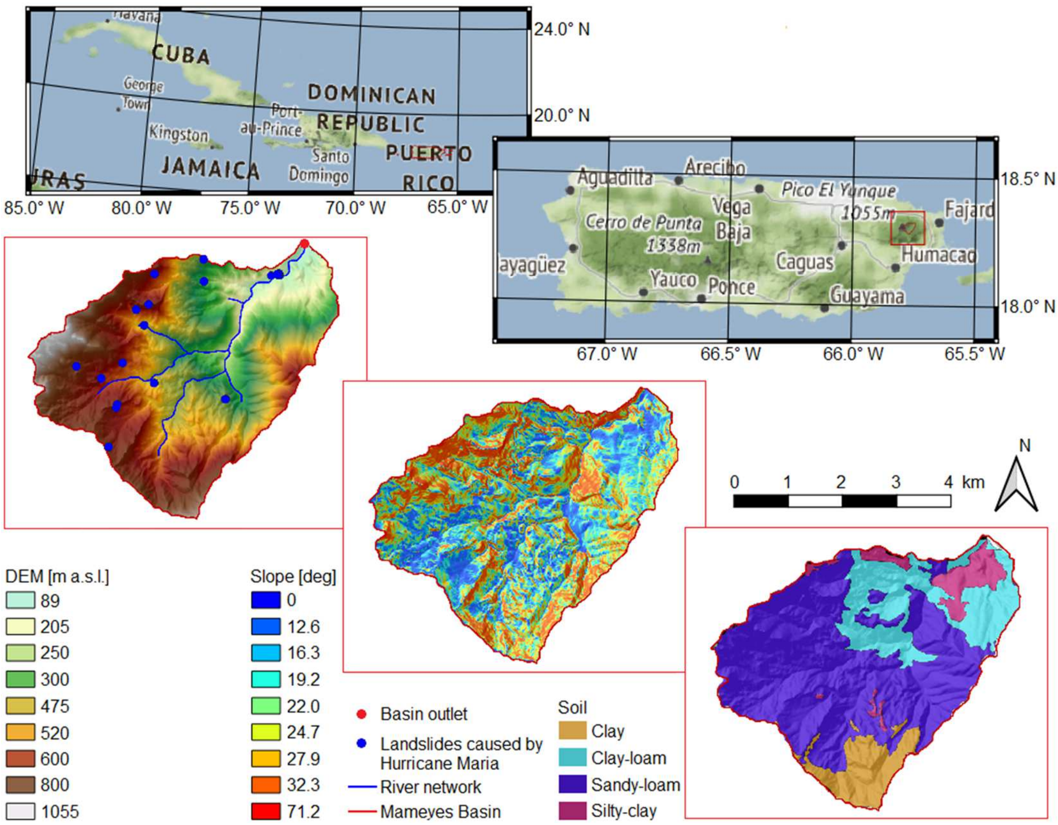

a)

b)

Figure 1 – (a) Digital elevation model (DEM), slope, soil map and location of landslides caused by Hurricane Maria in September 2017 for the Mameyes basin. (b) Images of landslides along the PR-191 and observed during a field trip in 2014. An old landslide with new vegetation is also shown (*pictures taken by Drs. Arnone and Dialynas*).

3.2 *Input data and model parameters*

The tRIBS-VEGGIE-Landside model requires meteorological forcing, soil distribution data, and soil and ecological parameters.

The used meteorological data and model parameters are those already obtained and calibrated for the Mameyes basin in previous studies by Lepore et al. (2013) and Arnone et al. (2016b). Specifically, the meteorological data derive from the Bisley Tower located within the basin (lat. 18.31, long. 65.74, 352 m a.s.l.), which measures many of the needed input data with an hourly resolution (wind speed and direction, air temperature, cloud cover, relative humidity, rainfall, and incoming shortwave radiation). We used the same rainfall forcing as in Lepore et al. (2013), corresponding to the period between January and November 2008, which includes an important event that occurred in April 2008. Specifically, we analyzed the results obtained over a time window of 48 hours encompassing the event recorded between the 27 and 28 April 2008 with a peak rainfall intensity of about 100 mm/h at $t = t_p$ (Figure 2). The model operates continuously at the hourly scale.

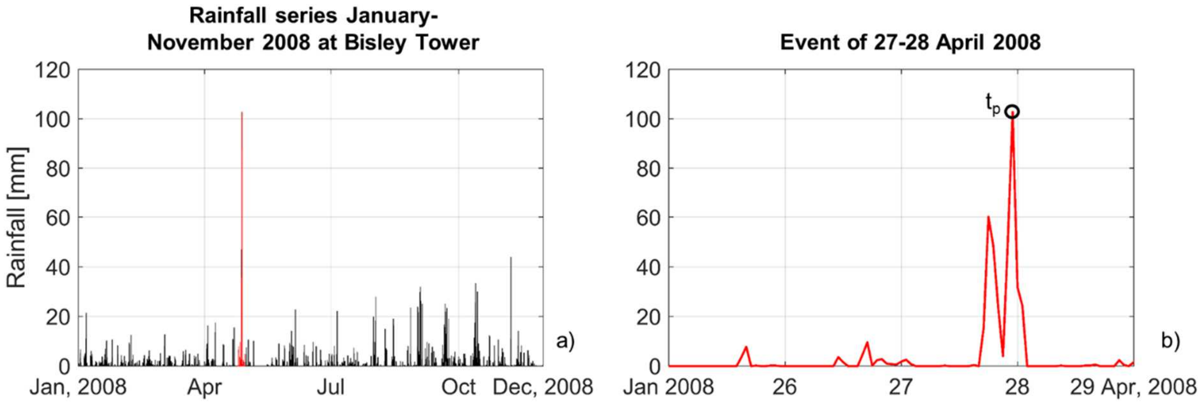

Figure 2 – (a) Rainfall recorded at the Bisley Tower for the period January-November 2008 (black curve) with a focus on the rainfall event of 27-28 April 2008 (red curve), which was analyzed to explore the changes in soil moisture pattern and soil instability. Panel (b) focuses on the analyzed event, where the time of the storm peak is denoted as t_p.

As described in Lepore et al., (2013), soil data were extracted from the soil map retrieved from the USDA Forest Service's International Institute of Tropical Forestry of San Juan. Additionally, a calibration procedure of the main hydrological soil parameters was conducted by the authors based on soil moisture time series from May to November 2008 observed at three locations, within an area close to the Bisley Tower. Values of main hydrologic and soil parameters are reported in Table 1, which are constant across the five model configurations (which will be introduced in the next section). It is important to highlight that landslide-model related parameters were not calibrated.

Table 1. Main hydrological and mechanical soil properties. Source Lepore et al., (2013).

Parameter	**Description**	**Units**	**Clay-loam**	**Sandy-loam**	**Silty-clay**	**Clay**
K_s	Saturated hydraulic conductivity	[mm/h]	50.0	50.0	30.0	10.0
θ_s	Saturated soil moisture	[mm^3/mm^3]	0.56	0.55	0.55	0.53
θ_s	Residual soil moisture	[mm^3/mm^3]	0.075	0.041	0.051	0.09
λ	Pore size distribution index	[-]	0.2	0.32	0.13	0.13
ψ_b	Air entry bubbling pressure	[mm]	-250	-150	-340	-370
φ	Soil friction angle	[deg]	25	25	25	25
c'	Soil effective cohesion	[N/m^2]	3000	3000	3000	3000
A_r	Anisotropy ratio	[-]	1÷300	1÷300	1÷300	1÷300

Parameter A_r is responsible of the lateral redistribution of soil moisture, which has been reported to be significant in the Mameyes basin (Harden and Delmas Scruggs, 2003). A_r, which is defined as the ratio between saturated hydraulic conductivities in the directions parallel and normal to the slope (K_s), partially controls the lateral subsurface flux transfer. A_r was varied from 1 to 300 (Table 1). Values used are reported in the model setup section. Mechanical parameters, i.e., effective soil cohesion, *c'*, and friction angle, ϕ, are reported in Table 1 (sources: Lepore et al., 2013; Simon et al., 1990).

Finally, with regard to the topography data, calibration of the parameters mentioned was done using the 30 m resolution DEM available for the island of Puerto Rico to derive the TIN network. This study, uses the now available 10 m resolution DEM as the core data set for the resolution studies, as described in the next section.

3.3 *Model setup*

Resampled DEMs at resolutions of 20, 30, 50, and 70 m were obtained from the 10 m DEM by applying the nearest neighbor interpolation technique, which does not alter any of the values of cells from the input grid and assigns the value of the cell centers on the input grid to the closest cell center on the output grid (Figure 3, first column). Indeed, others have argued that limited to hydrological applications, the nearest neighbor technique leads to the highest accuracy in DEM resolution resampling (Takagi, 1998; Tan et al., 2015; Wu et al., 2008).

The five DEMs were then used to derive the corresponding hydrologically-significant TINs mentioned in section 2.2. Specifically, the combination of Slope Criteria and LT sampling method was used for each configuration; the method retains a number of significant nodes corresponding to the *TIN to DEM ratio*, ν, in order to obtain a reasonable balance between a feasible computational cost and an efficient preservation of topographic characteristics. Therefore, the percentage of retained points with such a choice is the one that guarantees the best hydrographic similarity. Specifically, the aim is to preserve the catchment slope distribution, as well as the hydrographic features. As the DEM resolution decreases, the ratio ν required to preserve topographic attributes increases. Finally, from the TIN-nodes, the Voronoi polygons are uniquely defined. Table 2 summarizes the characteristics for each configuration.

Table 2. Number of DEM cells, TIN nodes, and Voronoi polygons for each DEM resolution. Because some nodes are used as catchment boundaries, the final number of Voronoi polygons is lower than the TIN nodes.

DEM Resolution [m]	#DEM cells	#TIN nodes	TIN to DEM ratio, ν	#Voronoi polygons
10	169,615	6,974	4%	6,276
20	42,400	3,605	9%	3,131
30	18,837	2,603	14%	2,190
50	6,782	2,274	34%	1,908
70	3,462	2,416	70%	2,177

Special attention is paid to the spatial distribution of the slope, since the slope controls the hydrology and the soil stability and its estimation is affected by DEM resolution (Chang and Tsai, 1991; Claessens et al., 2005; Grohmann, 2015; Arnone et al., 2016a). For the sake of comparison, grid-based maps of slope are derived from each DEM using the planar method of average maximum technique on a 3x3 kernel (Burrough, 1998) implemented within ArcMap of ESRI.

Figure 3 illustrates the five DEMs (first column) and the Voronoi polygons together with their spatial distributions of slope. The figure shows that high resolutions capture more variability in DEM elevation. The grid-based maps of slope (second column) highlight a considerable smoothing of slopes at lower resolutions (e.g., 50 and 70 m), especially in the central and south areas of the watershed, where higher slopes (orange to red cells) are replaced in some cases by gentler slopes (blue cells). This smoothing is less evident on the Voronoi-based maps (third column). According to the Voronoi contours, it is noteworthy to observe that gentler slope areas of the watershed are represented by large Voronoi elements (blue polygons), while in steeper areas topographic variability is better described by more and smaller Voronoi elements (orange/red polygons).

The lost in accuracy in the description of topography may lead to a different watershed divide and a slightly smaller watershed area (i.e., 50 and 70 m Voronoi mesh). However, since the analyses will be mostly conducted at a basin scale, this will not undermine the results.

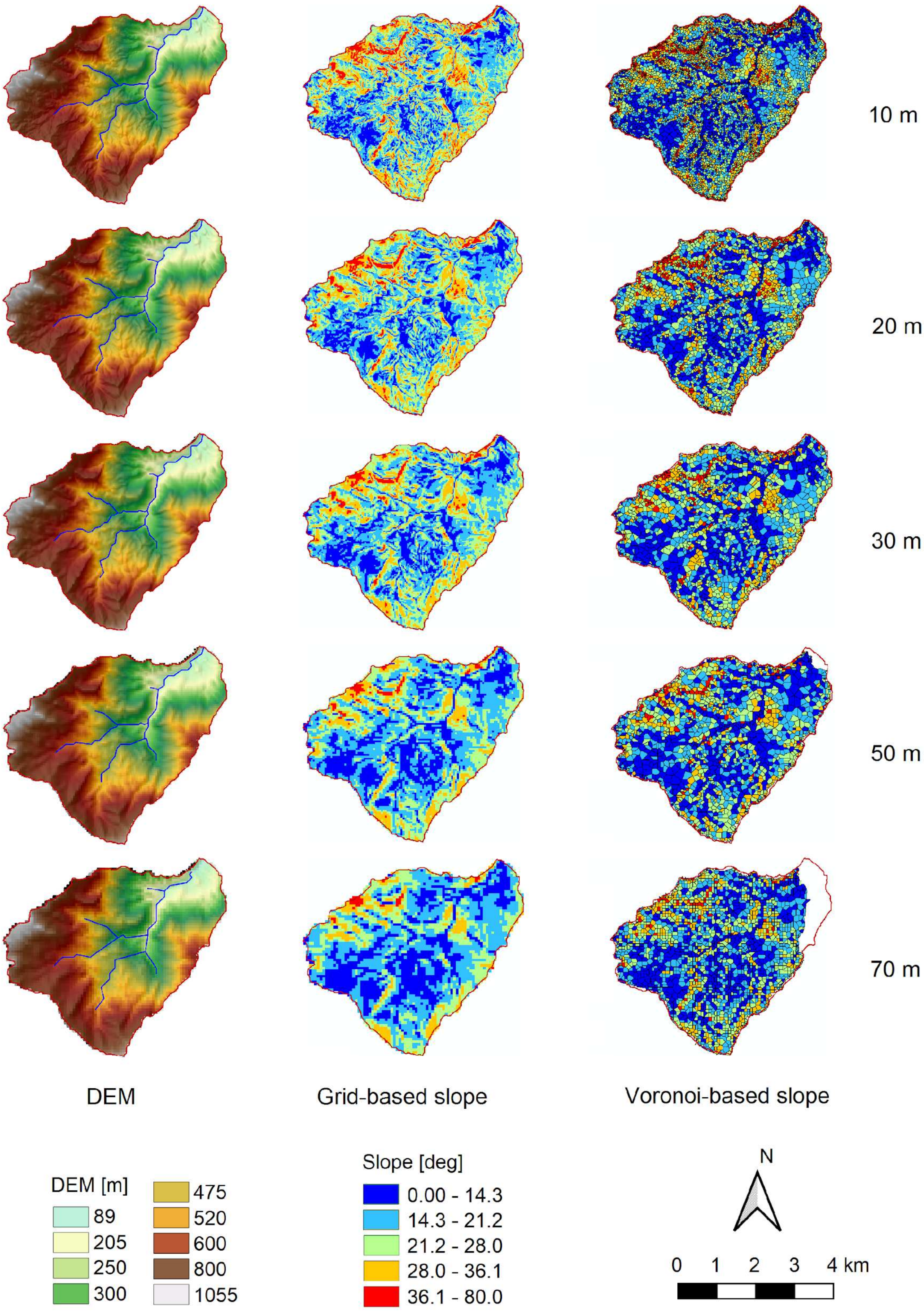

Figure 3 – DEM, slope derived from DEM (grid-Slope), and slope on Voronoi polygons (Voronoi Slope) as generated in TIAP from different resolutions of DEM (e.g., 10, 20, 30, 50, and 70 m) for the Mameyes basin.

Table 3 lists some basic statistics (i.e., minimum, maximum, mean, median, and standard deviation) of the area and slope of Voronoi polygons, together with the slope of grid cells, for the different resolutions. It is observed that the Voronoi-based maps tend to provide higher maximum slope values. This can be the result of the different algorithms used to calculate the slope with DEMs and Voronoi meshes, as discussed in section 3.3 and 2.2, respectively. Indeed, the use of an average maximum technique in the grid-based map tends to produce a smaller maximum gradient because of smoothing.

Table 3. Values of maximum (Max), minimum (Min), median, mean, and standard deviation (St. Dev.) for the Voronoi polygons area and the Voronoi/grid slope as a function of DEM resolution.

	Voronoi Area [m^2]					**Voronoi/grid Slope [deg]**				
DEM Resolution [m]	**Min**	**Max**	**Mean**	**Median**	**St. Dev.**	**Min**	**Max**	**Mean**	**Median**	**St. Dev**
10	18	23,940	2,669	2,193	2,160	0.0/0.0	80.0/71.3	22.3/22.4	21.6/21.9	11.2/8.5
20	55	51,712	5,339	4,450	4,231	0.0/0.4	79.9/66.9	21.4/21.7	20.8/21.3	11.2/7.8
30	151	64,733	7,611	6,389	5,912	0.0/0.6	76.6/59.5	20.7/21.0	20.0/20.6	11.1/7.7
50	117	49,218	8,649	7,293	6,287	0.0/0.2	78.7/54.7	20.3/19.6	19.4/19.1	11.5/7.3
70	356	39,343	7,181	6,737	3,651	0.0/0.2	57.3/56.0	18.6/18.5	18.6/18.1	9.0/7.0

With regard to the Voronoi mesh derived from the 70 m DEM, a greater number and more regular Voronoi polygons were created as compared to the 50 m Voronoi mesh; this is explained by the need to retain more points in order to preserve the elevation description (ν ratio in Table 2).

Finally, we analyzed the results associated with the two extreme values of coefficient of anisotropy, i.e., $A_r = 1$ and $A_r = 300$ (Lepore et al., 2013). The selected coefficients of anisotropy are representative of two opposite situations: (i) water lateral redistribution is limited and the wetting front propagates mainly through infiltration, in the direction perpendicular to the terrain surface; (ii) there is a strong lateral redistribution, mainly driven by gravity.

4 Results

Slope stability in the model depends on terrain representation and simulated hydrological processes, both dependent on resolution. For given mechanical soil properties, three variables influence the local failure: depth of hypothetical plane of failure, slope, and soil moisture.

4.1 *Significant Lateral Redistribution (A_r = 300) Case*

The relation among the above-mentioned variables at failure conditions are shown in Figure 4, for A_r = 300, for the five parent DEM resolutions and at the time of the storm peak ($t = t_p$), which is representative of rapid changes in hydrological processes across soil depths.

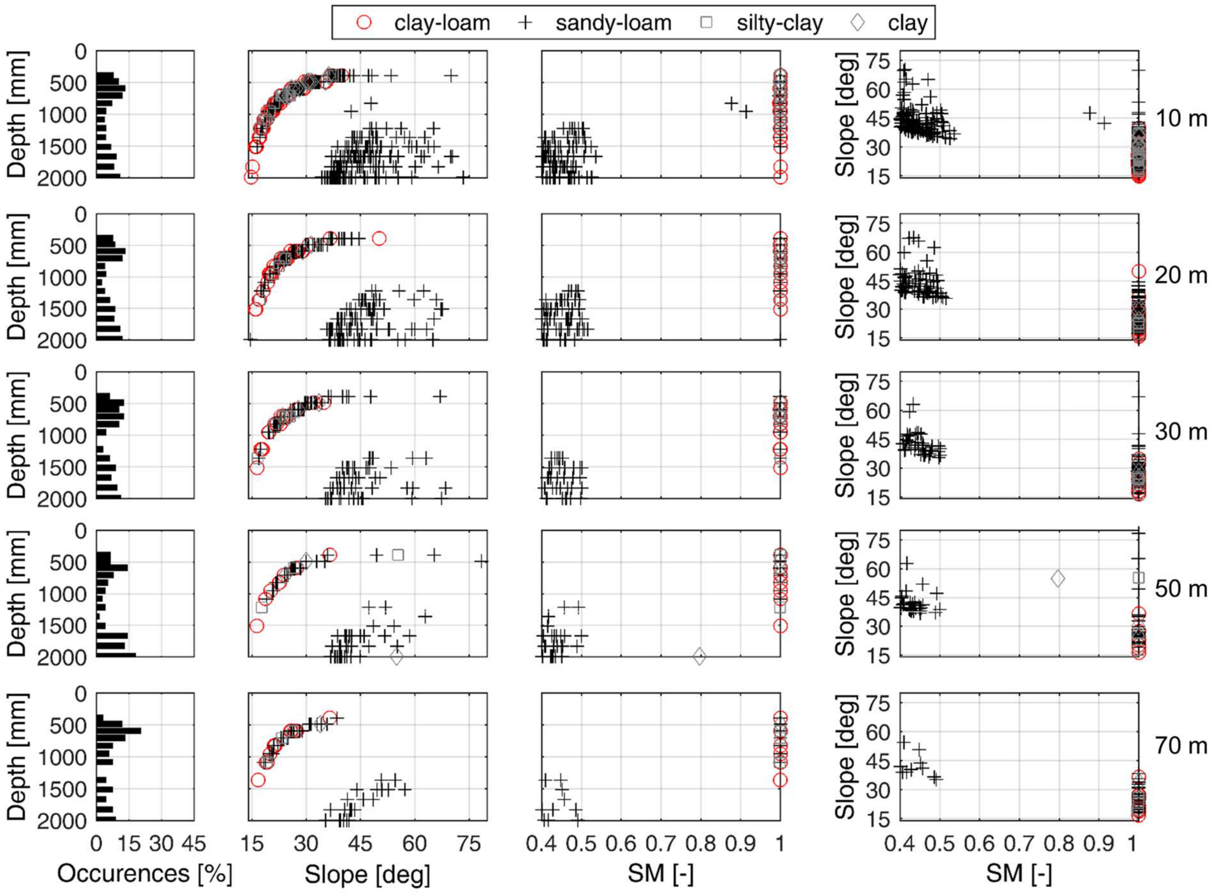

Figure 4 – Occurrences of depths of failure (first column); relation between depth of failure and slope (second column), depth of failure and normalized soil moisture (SM) (third column) and between slope and SM (fourth column) for the elements with $FS \leq 1$, at the time of the storm peak $t = t_p$, for the five parent DEM resolutions and A_r=300. Markers distinguish the soil types.

The panels on the first column report the frequency distribution of the depths of the plane of failure across the basin. Second and third panels show the scatterplots between the depth of failure and the slope and between the depth of failure and the normalized soil moisture (SM, or effective saturation) at failure, respectively. Finally, the panels on the fourth column show the relation between slope and SM. Elements characterized by different soil types are distinguished by different markers.

All the scatterplots in Figure 4 delineate two clear clusters of points describing different conditions. In one case, failures occur when the soil is saturated; such condition of failure is reached throughout the basin. Failure due to saturation occurs for all types of soil and mostly at shallow layers (i.e., between ~500 mm and ~1,000 mm), as denoted by the frequency distribution of the depths of failure. Under saturation, failures occur at moderate slopes i.e., within the range of ~15-35 deg.

A second cluster is formed by those polygons that are characterized by a slope greater than ~35 deg and fail mostly at depths greater than 1,250 mm; this only occurs over the sandy-loam soil (+ markers) where a low degree of saturation is reached. In unsaturated soil conditions the role of apparent cohesion due to soil matric suction (i.e., third term of eq. 1) can be significant (Lepore et al., 2013) but in sandy-loam there is a relatively (compared to other fine soils) small contribution of the apparent cohesion, described by the low absolute value of the air entry bubbling pressure (ψ_b, see Table 1). Thus, the elements in sandy-loam result in a failure even at unsaturated conditions and at deep failure depths, for the given geo-mechanical properties.

As the resolution degrades, from top (10 m) to bottom (70 m) panels, the two clusters can still be clearly distinguished, with less elements exhibiting slope failures as the resolution degrades and with fewer failing polygons having a very steep slope (e.g., greater than ~45deg), especially in the 70 m DEM-derived mesh.

Additionally, in contrast to the finest resolutions, which show failure surfaces at all depths, the coarser resolutions are characterized by shallow failures (across the all types of soils) and deep layers (mostly on the sandy-loam soil at unsaturated conditions, as previously explained).

Polygons that reach saturation fail mostly at depths of ~1,000 mm, or less.

The way depth, slope, and SM at failure are related to each other depends on the main topographical features, i.e., local slope and drainage polygons area, which influence the evolution of the hydrological processes and ultimately the slope instability. Therefore, these relations are associated to the accuracy in the description of the topographical features which varies with the five DEM-derived meshes.

Figure 3 showed that the TIN generation algorithm creates an implicit mutual dependence between areas and slopes of Voronoi polygons, with larger polygons describing gentler slope zones and smaller polygons describing more complex morphologies and hydrological significant areas, such as the river networks (Vivoni et al., 2005). An overview of this dependency for the five DEM-derived meshes is given in Figure 5, which shows the bivariate frequency distributions between area and slope of the Voronoi polygons. The distributions are assessed through the *Multivariate Kernel Density Estimation* (MKDE - Simonoff, 2012). The red area, the red + the orange area, and the sum of the red, orange, and yellow areas represents the 25%, 50%, and 75% of the bivariate distribution mass, respectively.

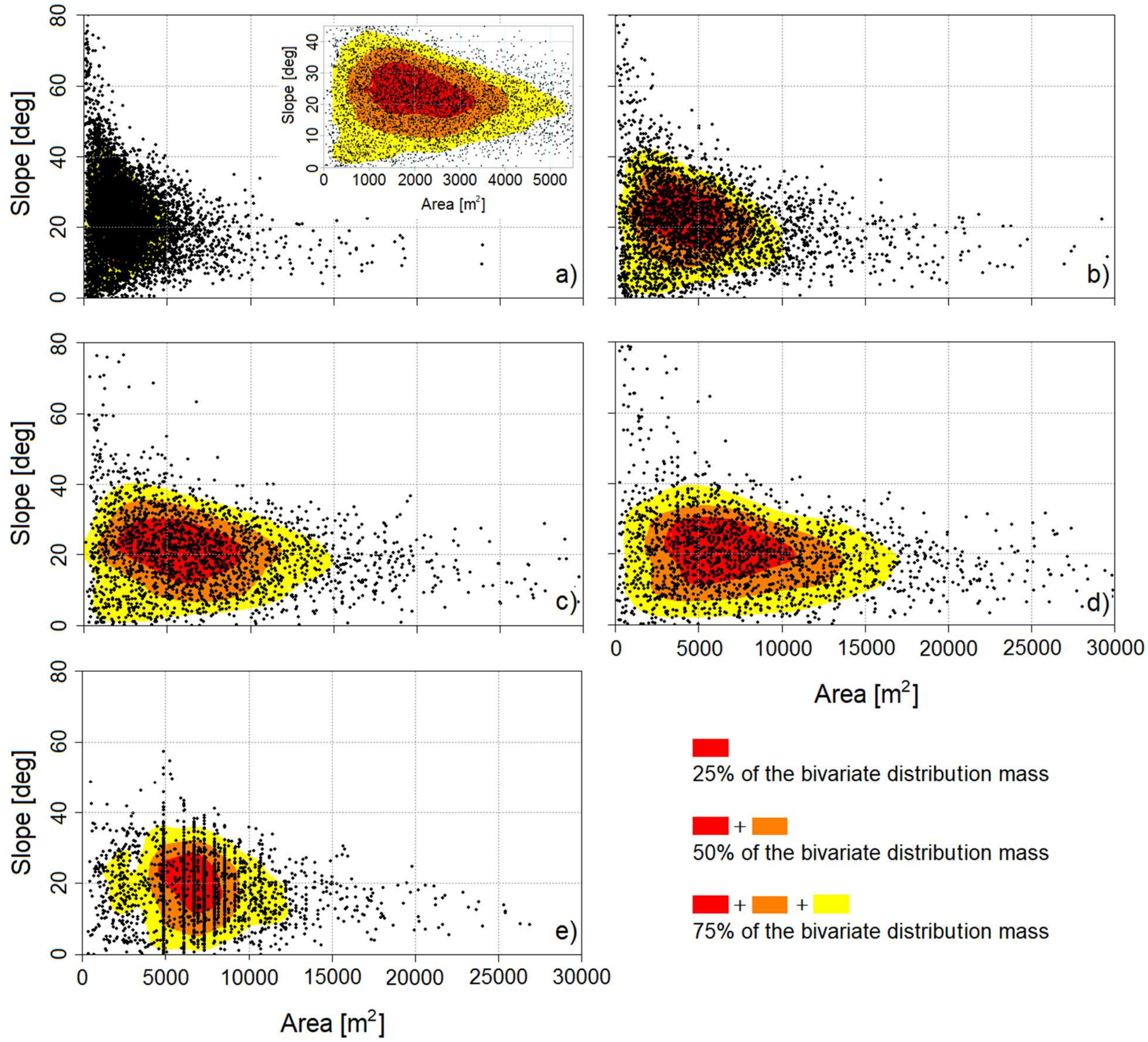

Figure 5 – The Multivariate Kernel Density Estimation of the area and slope of the Voronoi polygons at the resolutions of (a) 10 m, (b) 20 m, (c) 30 m, (d) 50 m, and (e) 70 m; red = 25%, red + orange = 50%, red + orange+ yellow = 75% of the bivariate distributions mass, respectively.

The distribution of the points corresponding to the Voronoi polygons derived from the parent 10m DEM clearly shows the presence of very steep elements (> 60 deg) that are represented by very small polygons, and of a few elements corresponding to very large polygons drawn for zones at moderate slope (between nearly flat areas and ~20 deg). As it is possible to notice from the inset of Figure 5a, 75% of generated polygons have an area ranging between 0 and ~5,000 m^2 and a slope lower than ~45 deg. Many of the very small and flat polygons describe the drainage network areas (see Figure 3). As the resolution of the parent DEM decreases, the probability mass spreads out towards larger Voronoi polygons areas, implying an increase in variability. Moreover, the center of the bivariate distribution slightly moves towards higher values of areas and lower values of slope. At the lowest resolution (Figure 5e) the variability in Voronoi polygons area decreases and slope values are smaller, with the absence of values greater than 60 deg, thus indicating a pronounced smoothing of the topography. Moreover, it is noteworthy the alignment of some points on the same vertical straight lines (Figure 5e) due to the regular shape of the resulting Voronoi polygons (see Figure 3). As previously mentioned, this result reflects the inability of TIAP to generate, from a too coarse DEM, a suitable irregular mesh that appropriately represents the topography of the basin.

The slope-area dependence of Voronoi polygons directly affects the spatial distribution of the modeled failures. The steepest areas of the basin, which are those most prone to fail, are represented by very small polygons only in the fine resolutions. The maps of the landslides at $t=t_p$ and for A_r=300 for the all meshes generated are shown in Figure 6. The north-western part of the basin is the area that exhibits greater occurrence of slope failures. It can be observed that the amount of such failures (i.e., black Voronoi polygons) gradually decreases as the resolution decreases. Additionally, polygons that fail (colored black) are smaller in the 10 m resolution mesh. The number, position and dimension of failing polygons across different resolutions is related to the different slope-area dependence depicted in Figure 5; failures in the 10 m resolution mesh originate mainly from small Voronoi elements associated to the highest slopes (Figure 5a) whereas the failures at the lowest resolution are associated to fewer and larger polygons characterized by slope higher than ~35° (Figure 5e), mainly in sandy-loam.

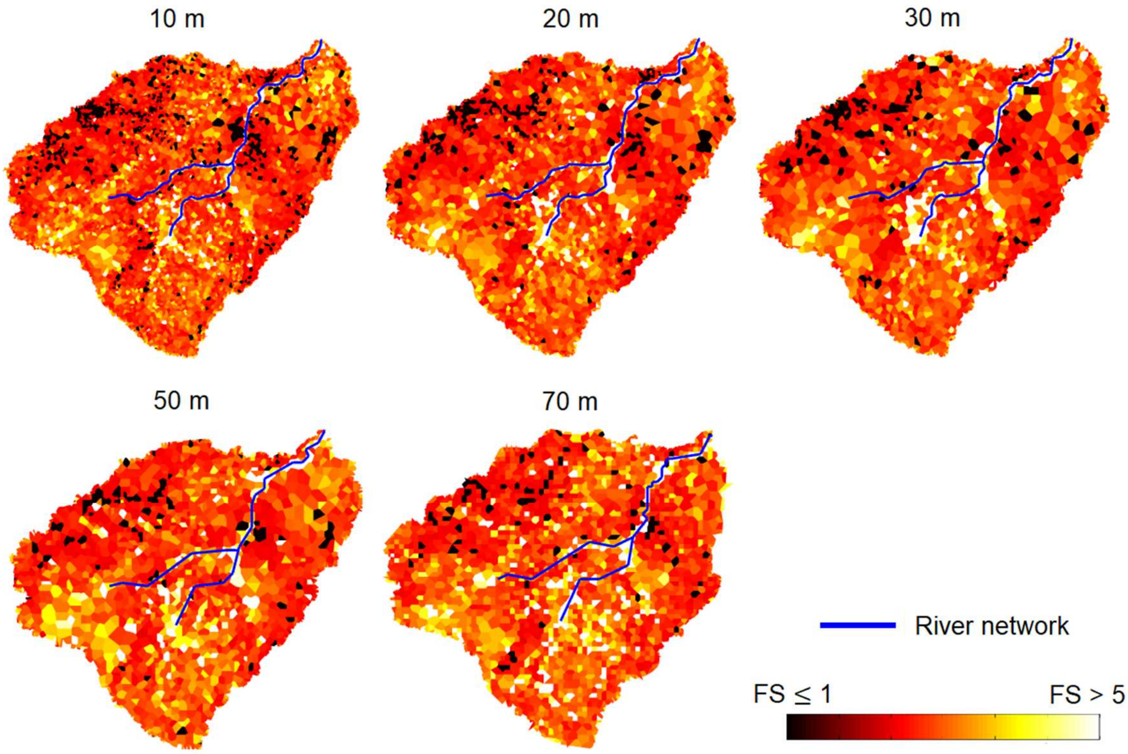

Figure 6 – Spatial distribution of the polygons at failure (black polygons) at the time of the storm peak $t=t_p$, for the five parent DEM resolutions and for A_r=300.

The resulting percentage of total area at failure is reported in Figure 7a; specifically, the inset histogram reports the percentage of total area at failure as a function of original DEM size. The main histogram depicts the relative total failure areas as a percent of the 10 m case, here taken as reference.

The main histogram shows that there is a clear reduction in percentage of total failure area as the parent DEM resolution is degraded. The simulation carried out using the 10 m DEM predicted that more than 7% of basin area is unstable. The simulations based on 20 m and 30 m DEMs predicted about 6% of the basin as unstable (around 80% of the 10 m DEM results). Finally, when 50 m and 70 m DEM resolutions are used, only about 3% of the basin area is classified as unstable (~ 40% of the 10 m DEM). This means that adopting a 50 m or 70 m DEM-derived resolution mesh leads to an underestimation of failure area of about 60% with respect to the highest resolution (10 m), considered as the more realistic scenario.

In terms of angle of failure (Figure 7b), the median varies considerably across the resolutions within the range 28-40 deg, whereas the variability is similar across all resolutions except for the coarsest resolution DEM, where it is somewhat smaller.

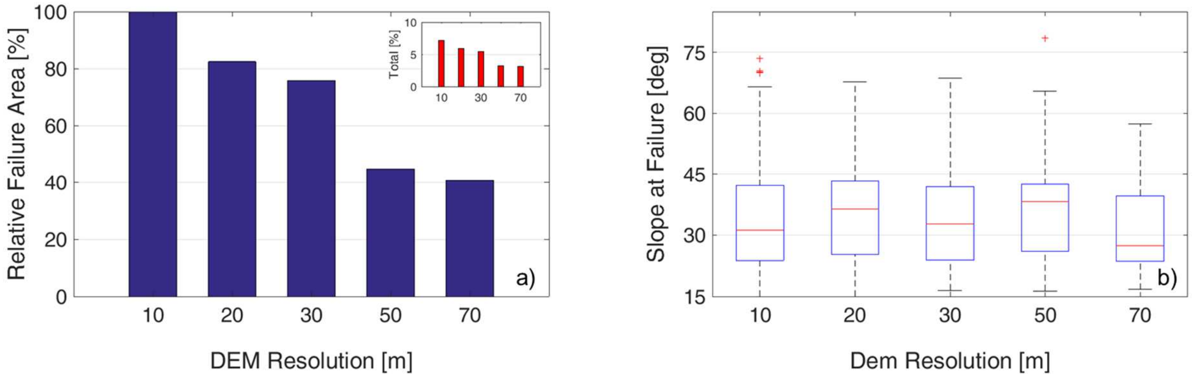

Figure 7 – Changes in percent of failure area and percent relative failure area (a) and slope at failure (b) at the time of the storm peak t=t_p, across the five parent DEM resolutions and for A_r=300. The small histograms at the top-right corner (a) report the percentage of total area at failure as a function of the parent DEM resolution, whereas the main histogram depicts the relative total failure as a percent of the 10 m case, here taken as reference (100 %).

As previously mentioned, besides the direct impact of slope on the triggering mechanisms of a landslide, the slope, and the accuracy in its representation, also have an indirect influence given that some of the hydrological processes that influence the soil moisture pattern are gravity driven. Figure 4 illustrates a decrease in the occurrence of moderate depths of failure, i.e., around 1,250 mm, as the resolutions degrades, especially at the 70 m DEM-derived mesh. In this case, apart from the unstable areas characterized by a sandy-loam soil type, which mostly fail for morphological and geo-mechanical reasons (since the soil is unsaturated), the rest of areas with slope greater than a certain value (~15 deg) become unstable because they reach saturation down to a certain critical depth. Specifically, the gentler the slope, the deeper the location of the depth of failure. However, in the case of coarser resolutions and particularly the 70 m parent DEM, very few elements fail because of saturation at depths greater than ~1,500 m (Figure 4). For the sake of process understanding, Figure 8 shows, for all polygons, the evolution of the soil moisture with depth for the coarsest (70 m) and finest (10 m) resolutions, reporting the scatterplot of slope vs soil moisture across the two soil types (i.e. clay-loam and sandy-loam), where most of the failures occur (Figure 4), for t=t_p, A_r=300, and at three soil depths, i.e., 500 mm (Figure 8a), 1,000 mm (Figure8b) and 2,000 mm (Figure 8c).

At a depth of 500 mm (Figure 8a), for the 70 m resolution (red marks) almost the entire basin is quasi-saturated (SM > 0.9). Whereas for the 10 m resolution (black marks), there is a greater number of Voronoi polygons that are not as saturated (SM < 0.9), especially at the steepest areas (slope > 60 deg). This condition explains why, at this time, failures occur mainly at shallow depths in the case of 70 m resolution (see Figure 4). Moving from 500 mm (Figure 8a) to 1,000 mm (Figure 8b) and to 2,000 mm (Figure 8c), it is possible to discern the movement of the front of infiltration in both resolutions. Indeed, the cloud of points moves from saturation (at the top of the soil column, Figure 8a) to drier values (at deeper soil horizons, Figure 8b and 8c), where the front of infiltration has not yet reached, especially in the 70 m resolution case. In fact, except for a single polygon, there are no saturated areas steeper than 20 deg, thus explaining the absence of failures due to saturation at depths deeper than ~1,250 mm (see Figure 4). Analysis of the same plots (not reported here) right before and after t_p confirmed such a movement of the moisture front. In this case, redistribution occurs and soil moisture spatial patterns are mainly controlled by topography.

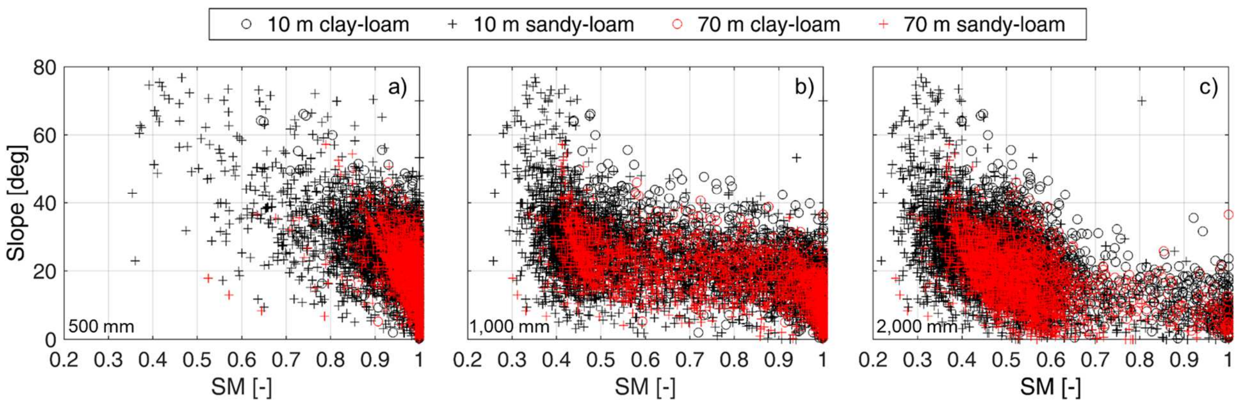

Figure 8 – Scatterplot of slope vs level of saturation (SM) for the 10 m (black) and 70 m (red) parent DEM resolutions, in clay-loam (o) and sandy-loam (+), at t=t_p and for A_r=300. Plots correspond to depths of (a) 500 mm,

(b) 1,000 mm and (c) 2,000 mm.

4.2 *Limited Lateral Redistribution (A_r = 1) Case*

When lateral redistribution of soil moisture is limited, such as in the case of anisotropy ratio A_r=1, the wetting front follows a considerably different path, as widely discussed in Lepore et al. (2013). Since the lateral exchanges are attenuated, the front of infiltration is mainly along the direction perpendicular to the soil surface (Lepore et al., 2013). Indeed, the above discussed scatterplots are significantly different for the case of A_r=1, as shown in Figure 9 for both the finest and coarsest resolutions and for the same two soil types of Figure 8. Specifically, down to 500 mm (Figure 9a), the basin is mostly saturated, regardless the soil type and the slope (except that for the very steep areas, i.e., slope > ~60 deg).

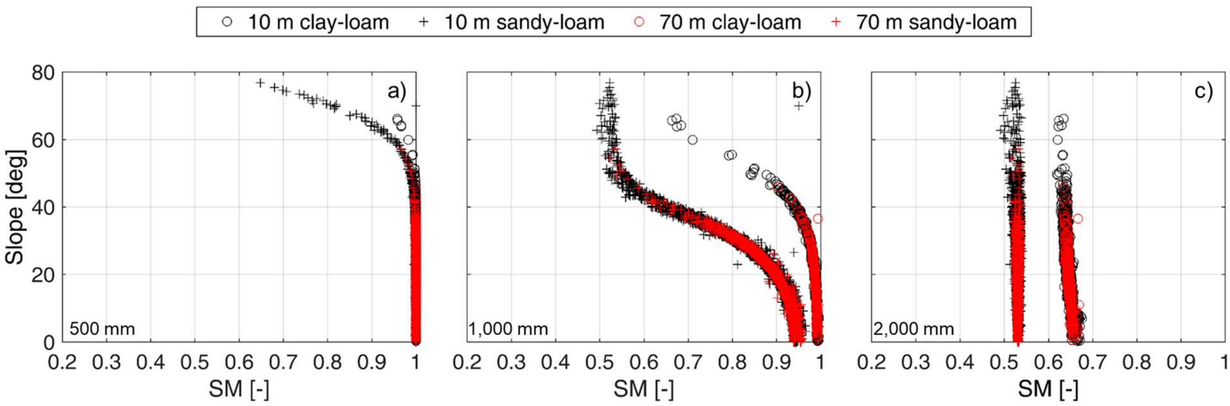

Figure 9 – As in Figure 8 but for A_r=1.

At larger depths (Figure 9b and 9c) it is possible to clearly distinguish the behavior of the two soil types, which are characterized by different water retention properties (see Table 1). Specifically, at the depth of 1,000 mm (Figure 9b), SM depends on slope following a nearly monotonic relationship; in this case, the local slope controls the propagation of vertical fluxes downwards the soil column within a single Voronoi element, together with the hydraulic conductivity properties. At the depth of 2,000 mm, SM mostly depends on soil type (Figure 9c), likely because the wetting front has not yet reached these deeper horizons. In this case, the changes in the slope representation with different meshes have less impact on the spatial soil moisture dynamics. This is likely because fluxes across contiguous polygons are minimized and the slope of a Voronoi element may not directly control the moisture dynamics of neighboring cells.

Figure 10 shows the results relative to the elements that fail for the finest (10 m) and coarsest (70 m) cases, for $t=t_p$ and $A_r=1$. As for the $A_r=300$ case, two clusters of points can be distinguished: (i) failures are triggered by the reaching the soil saturation and occur at very shallow horizons and moderate slopes; this happens mainly in the clay-loam soil and is more emphasized when the coarsest resolution is used; (ii) failures mainly occur in areas with critical slope (greater than ~35 deg) and a degree of saturation greater than 0.5. This situation occurs mainly in the sandy-loam soil and is attenuated in the 70 m DEM derived mesh because of its smoothed topography, as discussed before. With respect to the high anisotropy case, the greatest percentage of landslides is very shallow and thus attributable to the soil that reaches the saturation. In fact, the elimination of lateral redistribution of moisture, as previously discussed, leads to locally higher soil moisture.

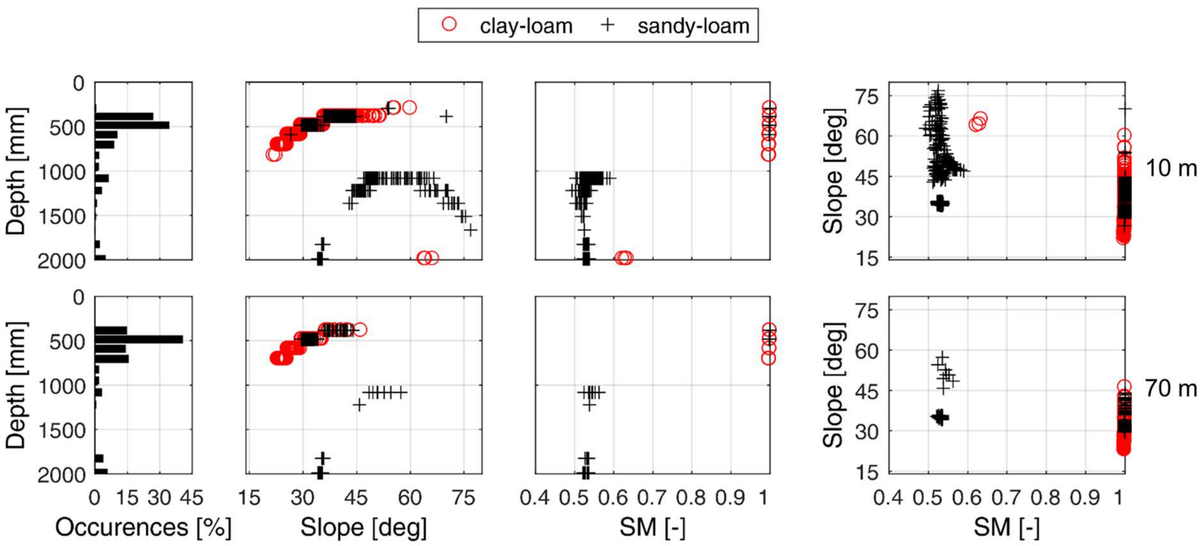

Figure 10 - Occurrences of depths of failure (first column); relation between depth of failure and slope (second column), depth of failure and normalized soil moisture (SM) (third column) and between slope and SM (fourth column) for the elements with $FS \leq 1$, at the time of the storm peak $t=t_p$, for $A_r=1$ and for the finest (10 m) and coarsest (70 m) parent DEM resolutions. Only clay-loam and sandy-loam soil types are represented.

The percentage of total areas at failure and slope at failure for the case A_r=1 is reported in Figure 11. The results show a percentage of failure area ranging from ~20%, for the case based on the 10 m original resolution, to ~10%, for the 70 m original resolution (Figure 11a). The higher percentage of failure area, as compared with A_r=300 (Figure 7a), demonstrates that, for given morphological features and rainfall trigger, the impacts of the hydrological processes (in this case the lateral redistribution) in reducing the soil saturation may be significant for the stability of the slope. The choice of A_r=1 reduces the sensitivity of the predicted area of failure across resolutions. The use of 50 m and 70 m resolutions predicted ~70% and ~60% of the failure area of the 10 m case, respectively (versus 40% for the A_r = 300 case).

Finally, the median values of slope at failure, together with their variability, exhibits a slight decreasing trend as the resolution degrades (Figure 11b); this trend reflects the smoothing effect of the coarser resolutions on slope as highlighted in Figure 3 and Figure 5.

The differences observed between the two cases with A_r=300 and A_r=1 point out that, when the lateral redistribution is limited (i.e., A_r=1), land slope is more important than the impacts of soil moisture (hydrology) on the land failure mechanisms.

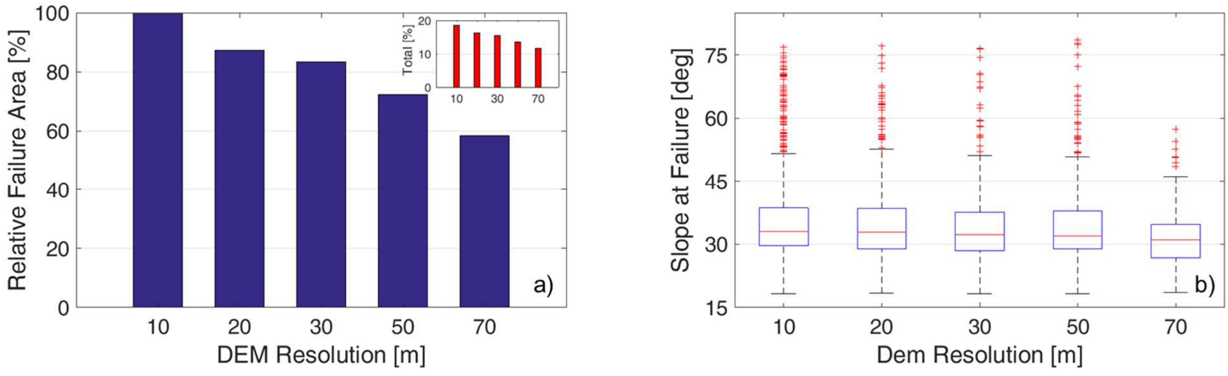

Figure 11 – As in Figure 7 but for A_r = 1.

5 Summary and Discussion

The effects of the original DEM size on the slope stability modeling have been explored by analyzing variables and processes that directly (i.e., slope) and indirectly (i.e., soil moisture dynamics) are involved in triggering failures. In contrast to other efforts, a distributed eco-hydrological-landslide model based on an irregular mesh, that is better suited to describe the topography, was used. A 10 m resolution DEM available for the study area was resampled to the resolutions of 20, 30, 50, and 70 m, in order to derive the corresponding hydrologically-significant TINs (Vivoni et al., 2004).

Slope is a terrain attribute derived from the DEM that directly influences the equilibrium of forces controlling the stability analysis. The steeper the slope, the greater are the forces that lead to the soil movement. Conversely, for given geo-mechanical properties of the soil, areas can be unconditionally stable (Montgomery and Dietrich, 1994; Arnone et al., 2011) below a certain value of slope.

The comparison with the grid-derived slope showed that the use of a triangulated mesh reduces the smoothing effect due to the use of coarse resolution grids (Chung and Tsai, 1991; Zhang and Montgomery, 1994; Claessens et al., 2015). With meshes as coarse as 30 m in resolution, the slope distribution is well preserved, especially in the range of slope values most critical for landslide modeling (i.e., slope greater than ~ 25 deg). A smoothing effect of the very steep slope values was observed only for the meshes derived from the 50 m and 70 m DEM resolutions (Figures 3 and 5).

The bivariate slope-area distributions of Voronoi polygons vary significantly among the five DEM-derived meshes (Figure 5). Specifically, as the resolution of the parent DEM decreases, the average area of the Voronoi polygons increases while the average slope value decreases, resulting in a smoothing effect of the topography. Because some of the modeled hydrological processes, such as convergence of fluxes and lateral redistribution, are directly controlled by the local slope (and the convergence areas), the variations in the bivariate slope-area distribution (Figure 5) are closely connected to the observed changes in the simulated hydrological behavior.

The Voronoi mesh derived from the 70 m resolution DEM constitutes an exception in the slope-area distribution, with points aligned on the same vertical straight lines (see Figure 5). These are mainly due to the excessive number of retained points from the original DEM that led to the creation of several similar Voronoi polygons. The result thus confirms the inability of generating, from a too coarse DEM, a suitable irregular mesh able to coherently represent the basin morphology (Vivoni et al., 2005) other than the shape of the watershed (Figure 3).

The polygons slope-area correlation arises only when irregular meshes are used, and thus this type of analysis is missing in work that is grid based (Tarolli and Tarboton, 2006; Claessens et al., 2015; Penna et al., 2014).

The combination of terrain description and simulated soil moisture dynamics determines the conditions of slope stability for each mesh resolution; specifically, we analyzed the dynamics at the time of the storm peak, representative of a time when the evolution of the hydrological processes is fast. The results can be summarized as follows:

- The smoothing effect of resolution on the description of topography leads to a reduction of the number of unstable polygons ($FS < 1$), especially when a 70 m DEM resolution is used.
- Failure due to saturation occurs at shallower layers as result of reaching saturation state rapidly, regardless of the resolution, as also found out by Viet et al. (2016). At the analyzed time of the simulation, shallow depths of failure are more frequent in the coarse resolution cases and, particularly, failures at the intermediate depths (~1,250 mm) are less frequent in the 70 m grid-size DEM compared to the 10 m case. This is because the combination of soil wetness and slope does not lead to FS values below the critical threshold; for example, in some cases the smoothing effect of the topography in the coarse resolution may lead to a high degree of saturation within the shallow horizons that reach the critical failure conditions; in other cases, at equal condition of saturation, the smoothing effect may reduce the local slope which then result to be not critical. The conditionally stable areas, i.e., those at intermediate slope (~ 15 deg, see Figure 4), are the ones affected by the changes in the resolution (Figure 4).

- The spatial distribution of simulated landslide locations (FS < 1) highlights the commonality across resolutions of areas of the basin most prone to instabilities; however, the 10 m case results in more elements and larger areas at failure (Figure 6).
- The quantitative analyses of failures confirm the decreasing trend in areas of failure as the resolution of the parent DEM decreases; this is particularly significant with the coarsest resolutions, i.e., 50 and 70 m, as shown by the relative assessment (Figure 7). The results agree with most of the previous studies, especially in highlighting that the changes are not necessarily linear with a loss of resolution, and that some degradation of resolution may be an acceptable compromise between the loss of accuracy in terrain description and the goodness of results (Fuchs et al., 2014; Penna et al., 2014; Tarolli and Tarboton, 2006; Dialynas, 2017).
- All the mechanisms that relate grid-size DEM with the simulated hydrological processes (e.g., mainly the SM lateral redistribution) are strongly smoothed if the anisotropy ratio A_r is equal to 1. Since in this case this parameter limits the gravity-driven process in the form of lateral exchanges (Lepore et al., 2013), the front of infiltration mainly develops along the direction perpendicular to the soil surface (Figure 9). For the specific case analyzed in this study, and for anisotropy ratio A_r=1, the changes in the soil moisture pattern leads to more Voronoi polygons resulting in a failure due to the higher degree of saturation of soil, especially at shallow soil horizons. In the case of A_r of 1, the landsliding process is dominated by the nature of infiltration and development of soil moisture fronts in each Voronoi polygon and hence less dependent on the the impact of lower resolution on the smoothing of the topography.

6 Conclusions

This study evaluated the hydro-geomorphological influences of DEM resolution on the slope stability analysis by using a distributed eco-hydrological-landslide model that uses a

Triangulated Irregular Network (TIN) to describe the topography. The model has been applied to the Mameyes basin (Puerto Rico), where numerous landslide analyses have been carried out in the past (Lepore et al., 2013; Arnone et al., 2016b).

The results demonstrated that the use of a TIN-based hydrological-landslide model can reduce the loss of accuracy in the derived slope distribution for coarse resolutions. Significant changes in the prediction of areas in failure result only when a very coarse DEM is used to derive the corresponding Voroni mesh and when the lateral redistribution of water, controlled by the anisotropy coefficient, is considerable. However, if the computational costs of the finest DEM resolution are prohibitive, the use of a slightly coarser resolution may be a good compromise to still identify the zones highly susceptible to landslides.

Future efforts can investigate how products of very high resolution, e.g., 1 m, could enhance the modeling of landslides in the Luquillo Experimental Forest by focusing on landslide phenomena in the road cut slopes.

Acknowledgements and data availability

Map of soil is available from the "Soil Survey of Caribbean National Forest and Luquillo Experimental Forest, Commonwealth of Puerto Rico", at the USDA Forest Service website www.nrcs.usda.gov. All data and calibrated parameters can be obtained from Dr. E. Arnone, elisa.arnone@uniud.it. The work of Dr. Dialynas while at the Georgia Institute of Technology and the collaboration with Drs. Arnone and Noto by Dr. Bras' research group has been supported by the National Science Foundation (Luquillo Critical Zone Observatory, Award EAR1331841). R. L. Bras acknowledges the support of the K. Harrison Brown Family Chair at Georgia Tech..

References

Arnone E., Francipane A., Scarbaci A., Puglisi C., Noto L.V. (2016°). Effect of raster resolution and polygon-conversion algorithm on landslide susceptibility mapping, Environmental Modelling & Software, 84: 467-481, https://doi.org/10.1016/j.envsoft.2016.07.016.

Arnone E., Dialynas Y.G., Noto L.V., Bras R. L. (2016b). Accounting for soils parameter uncertainty in a physically-based and distributed approach for rainfall-triggered landslides, Hydrological Processes 30, 927-944, 10.1002/hyp.10609.

Arnone E., Noto L. V., Lepore C., Bras R. L. (2011). Physically-based and distributed approach to analyze rainfall-triggered landslides at watershed scale, Geomorphology 133: 121-131.

Brooks, R.H. and Corey, A.T. (1964). Hydraulic Properties of Porous Media. Hydrology Papers 3, Colorado State University, Fort Collins, 27 p.Cama M., Conoscenti C., Lombardo L., Rotigliano E. (2016). Exploring relationships between grid cell size and accuracy for debris-flow susceptibility models: a test in the Giampilieri catchment (Sicily, Italy), Environmental Earth Sciences 75: 1-21.

Cavazzi, S., Corstanje, R., Mayr, T., Hannam, J. & Fealy, R. (2013). Are fine resolution digital elevation models always the best choice in digital soil mapping? Geoderma, 195–196, 111–121.

Chang K.T., Tsai B.W. (1991). The effect of dem resolution on slope and aspect mapping, Cartography and Geographic Information Systems 18: 69-77.

Ciampalini, A., Raspini, F., Frodella, W., Bardi, F., Bianchini, S., Moretti, S. (2016). The effectiveness of high-resolution LiDAR data combined with PSInSAR data in landslide study. Landslides (2016) 13:399–410.

Claessens L., Heuvelink G. B. M., Schoorl J. M., Veldkamp A. 2005. DEM resolution effects on shallow landslide hazard and soil redistribution modelling, Earth Surface Processes and Landforms 30: 461-477.10.1002/esp.1155.

Dialynas, Y. G. (2017). Influence of linked hydrologic and geomorphic processes on the terrestrial carbon cycle. PhD diss., Georgia Institute of Technology.

Dialynas, Y.G., Bastola, S., Bras, R.L., Marin-Spiotta, E., Silver, W.L., Arnone, E., Noto, L.V. (2016). Impact of hydrologically driven hillslope erosion and landslide occurrence on soil organic carbon dynamics in tropical watersheds. Water Resources Research, 52 (11), pp. 8895-8919

Francipane, A., Cipolla, G., Maltese, A., La Loggia, G., Noto, L.V. (2020). Using very high resolution (VHR) imagery within a GEOBIA framework for gully mapping: an application to the Calhoun Critical Zone Observatory. Journal of Hydroinformatics, 22 (1): 219–234. doi: https://doi.org/10.2166/hydro.2019.083.

Francipane, A., Ivanov, V. Y., Noto, L. V., Istanbulluoglu, E., Arnone, E., and Bras, R. L. (2012): TRIBS-Erosion: A parsimonious physically-based model for studying catchment hydrogeomorphic response, Catena, 92, 216–231.

Freer J, McDonnell JJ, Beven KJ, Peters NE, Burns DA, Hooper RP, Aulenbach B, Kendall C. (2002). The role of bedrock topography on subsurface storm flow. Water Resources Research 38: 1269.

Fuchs, M, Torizin, J., Kühn, F. (2014). The effect of DEM resolution on the computation of the factor of safety using an infinite slope model. Geomorphology 224 (2014) 16–26.

Goodrich, D. C., Woolhiser, D. A., and Keefer, T. O. (1991). Kinematic routing using finite elements on a triangular irregular network.Water Resour. Res., 27(6), 995–1003.

Grohmann C. H. (2015). Effects of spatial resolution on slope and aspect derivation for regional-scale analysis, Computers and Geosciences 77: 111-117.

Harden, C. P. and Delmas Scruggs, P. 2003. Infiltration on mountain slopes: a comparison of three environments, Geomorphology, 55, 5–24, 2003.

Hoeppe P., (2016). Trends in weather related disasters – Consequences for insurers and society. Weather and Climate Extremes, Volume 11, March 2016, Pages 70-79.

Ivanov, V., Bras, R. L., and Vivoni, E. R. (2008). Vegetation-Hydrology Dynamics in Complex Terrain of Semiarid Areas: II. Energy-Water Controls of Vegetation Spatio-Temporal Dynamics and Topographic Niches of Favorability, Water Resour. Res., 44, W03430.

Ivanov, Valeriy Y., Enrique R. Vivoni, Rafael L. Bras, and Dara Entekhabi. (2004a). Development of a triangulated irregular network model for real-time, continuous hydrologic forecasting, Water Resources Research, 40 W11102

Ivanov, Valeriy Y., Enrique R. Vivoni, Rafael L. Bras, and Dara Entekhabi. (2004b). Preserving, high-resolution surface and rainfall data in operationalscale basin hydrology: a fully-distributed physically- based approach, Journal of Hydrology, 298, 80-111.

Iverson, R. M. (2000). Landslide triggering by rain infiltration, Water Resour. Res., 36, 1897–1910.

Keijsers J.G.S., J.M. Schoorl, K.-T. Chang, S.-H. Chiang, L. Claessens, A. Veldkamp. (2011). Calibration and resolution effects on model performance for predicting shallow landslide locations in Taiwan. Geomorphology 133 168–177

Kumler, M. P. (1994). An intensive comparison of triangulated irregular networks (TINs) and digital elevation models (DEMs).Cartographica, 31(2), Monograph 45, 1–48

Lee M., Wang S., Lin T. 2010. The Effect of Spatial Resolution on Landslide Mapping - A Case Study in Chi-Shan River Basin, Taiwan,31th Asian Conference on Remote Sensing. Hanoi, Vietnam.

Lepore, C., Arnone, E., Noto, L. V., Sivandran, G., Bras, R. L. (2013). Physically based modeling of rainfall-triggered landslides: a case study in the Luquillo forest, Puerto Rico. Hydrol. Earth Syst. Sci. 17, 3371–3387.

Lee, J., (1991). Comparison of existing methods for building triangular irregular network models of terrain from grid digital elevation models. Int. J. Geograph. Inf. Sci., 5(3), 267–285.

Marsh, C.B., Pomeroy, J., Wheater, H.S., 2020. The Canadian Hydrological Model (CHM) v1.0: a multi-scale, multi-extent, variable-complexity hydrological model – design and overview.

Geosci. Model Dev., 13, 225–247Mita, C., Catsaros, N., and Gounaris, N. (2001). Runoff cascades, channel network and computation hierarchy determination on a structured semi-irregular triangular grid.J. Hydrol., 244, 105–118

Montgomery D. R., Dietrich W. E. (1994). A physically based model for the topographic control on shallow landsliding, Water Resources Research 30: 1153-1171.

Penna, D., Borga, M., Aronica, G. T., Brigandì, G., Tarolli, P. (2014).The influence of grid resolution on the prediction of natural and road-related shallow landslides. Hydrol. Earth Syst. Sci., 18, 2127–2139, 2014.

Rosso R., Rulli M. C., Vannucchi G. (2006). A physically based model for the hydrologic control on shallow landsliding, Water Resources Research 42: 16.10.1029/2005.

Mahalingam R., and Olsen, M.J., (2015). Evaluation of the influence of source and spatial resolution of DEMs on derivative products used in landslide mapping. Geomatics, Natural Hazards and Risk, doi.org/10.1080/19475705.2015.1115431.

Noto, L.V., S Bastola, YG Dialynas, E Arnone, RL Bras. (2017). Integration of fuzzy logic and image analysis for the detection of gullies in the Calhoun Critical Zone Observatory using airborne LiDAR data. ISPRS Journal of Photogrammetry and Remote Sensing 126, 209-224.

Tarolli P., Tarboton D. G. 2006. A new method for determination of most likely landslide initiation points and the evaluation of digital terrain model scale in terrain stability mapping, Hydrol. Earth Syst. Sci. 10: 663-677.10.5194/hess-10-663-2006.

Tarolli P, Dalla Fontana G (2009) Hillslope to valley transition morphology: new opportunities from high resolution DTMs. Geophys J Roy Astron Soc 113:47–56.

Tsai, V. J. D. (1993). Delaunay triangulations in TIN creation: An overview and a linear-time algorithm.Int. J. Geograph. Inf. Sci., 7(6), 501–524

Tucker, G. E., Catani, F., Rinaldo, A., and Bras, R. L. (2001). Statistical analysis of drainage density from digital terrain data.Geomorphology, 36, 187–202

Simon, A., Larsen, M. C., and Hupp, C. R. (1990). The role of soil processes in determining mechanisms of slope failure and hillslope development in a humid-tropical forest eastern Puerto Rico, Geomorphology, 3, 263–286.

Simonoff, J.S., (2012). Smoothing Methods in Statistics. Springer Science & Business Media. Singh, V.P., Woolhiser, D.A., 2002. Mathematical modeling of watershed hydrology. J. Hydrol. Eng. 7 (4), 270–292.

Sivandran, G. and Bras, R. L. (2012). Identifying the optimal spatially and temporally invariant root distribution for a semiarid environment, Water Resour. Res., 48, W12525.

Takagi, M. (1998). Accuracy of digital elevation model according to spatial resolution. International Archives of Photogrammetry and Remote Sensing, 32(4), 613-617

Tan M, Darren L. Ficklin, Barnali Dixon, Ab Latif Ibrahim, Zulkifli Yusop, Vincent Chaplot (2015). Impacts of DEM resolution, source, and resampling technique on SWAT-simulated streamflow, Applied Geography, 63, 357-368, ISSN 0143-6228

Vaze, J., Teng. J., Spencer, G. (2010). Impact of DEM Accuracy and Resolution on Topographic Indices. Environmental Modelling and Software 25(10):1086-1098.

Viet, T., Lee, G., Thu, T.M., An, H.U. (2016). Effect of Digital Elevation Model Resolution on Shallow Landslide Modeling Using TRIGRS. Nat. Hazards Rev., 04016011.

Vivoni, E. R., Ivanov, V. Y., Bras, R. L., and Entekhabi, D. (2004). Generation of triangulated irregular networks based on hydrological similarity, J. Hydrol. Eng., 9, 288–302.

Wang, L.J., Sawada, K., Moriguchi, S., (2013). Landslide susceptibility analysis using light detection and ranging-derived digital elevation models and logistic regression models: a case study in Mizunami City. Jpn. J. Appl. Remote Sens.. JRS.7.073561.

Watson, D. F., and Philip, G. M. (1984). Systematic triangulations. Comput. Vis. Graph. Image Process., 26, 217–223

Wu, S., Li, J. Huang, G.H. (2007). Modeling the effects of elevation data resolution on the performance of topography-based watershed runoff simulation. Environmental Modelling & Software 22, 1250-1260.

Wu S., Jonathan Li, G.H. Huang (2008). A study on DEM-derived primary topographic attributes for hydrologic applications: Sensitivity to elevation data resolution, Applied Geography, 28(3), 210-223

Yang P., Ames D.P., Fonseca A., Anderson D., Shrestha R., Glenn N.F., 2014. What is the Effect of LiDAR-Derived DEM Resolution on Large-Scale Watershed Model Results? Environmental Modelling & Software, 58, 48-57.

Zhang, W., Montgomery, D., (1994). Digital elevation model grid size, landscape representation, and hydrologic simulations. Water Resour. Res., 30 (4), pp. 1019-1028